Calculation of Spatial Response of a Collimated Segmented HPGe Detector for Gamma Emission Tomography by MCNP Simulations

Vikram Rathore, Lorenzo Senis, Peter Jansson, Erik Andersson Sundén, Ane Håkansson, and Peter Andersson

Abstract—We have proposed a planar electronically segmented high-purity germanium (HPGe) detector concept in combination with a multislit collimator for gamma emission tomography. In this work, the spatial resolution achievable using the collimated segmented HPGe detector was evaluated, prior to the manufacture and operation of the detector. The spatial response of a collimated segmented HPGe detector concept was evaluated using simulations performed with Monte Carlo N-Particle (MCNP) transport code MCNP6. The full detector and multislit collimator system were modeled, and for the quantification of the spatial response, the modulation transfer function (MTF) was chosen as a performance metric. The MTF curve was obtained through the calculation of the line spread function (LSF) by analyzing the simulated projection data. In addition, tomographic reconstructions of the simulated simplified test objects were made to demonstrate the performance of the segmented HPGe detector in planned application. For 662-keV photons, the spatial resolution obtained was approximately the same as the collimator slit width for both the 100- and 150-mm-long collimators. The corresponding spatial resolution at 1596-keV photon energy was almost twice the slit width for the 100-mm collimator, due to the partial penetration of the high-energy gamma rays through the collimator bulk. For a 150-mm-long collimator, an improved resolution was obtained.

Index Terms—Gamma emission tomography (GET), Monte Carlo N-Particle (MCNP), modulation transfer function (MTF), segmented high-purity germanium (HPGe).

I. Introduction

HIGH-PURITY germanium (HPGe) detectors are well-known for their excellent energy resolution and reasonably high detection efficiency in the gamma-ray spectrometry field. Because of these properties, HPGe detectors are widely used in many scientific applications. In nuclear structure studies, electronically segmented HPGe detectors have been used for gamma-ray tracking applications such as Advanced GAmma Tracking Array (AGATA) [1] and Gamma-Ray Energy Tracking In-beam Nuclear Array (GRETINA) [2]. A similar kind of segmented HPGe detector [3], [4] has also been proposed for gamma emission tomography (GET) of nuclear fuel. In particular, the GET technique has been used in the examination of nuclear fuel rods exposed to in-pile transient tests in material test reactors [5]–[7]. In such GET inspections, high spatial resolution is valuable for studying fragmentation, relocation, and dispersal of fuel from a fuel element or rod. The feasibility of segmented HPGe detector for GET instruments was evaluated through the simulation study in [3], and the detector geometry and segmentation pattern were optimized in [4].

Due to the promising results, an instrument is currently being manufactured for experimental demonstration. In this work, the demonstration device is presented, which is an electronically segmented HPGe detector similar to the proposed design in [3] and [4], albeit scaled-down with fewer segments and of planar geometry, to lower the costs of manufacturing. Aside from lower manufacturing costs of the detector itself, other reasons for choosing the scaled-down planar design for demonstration are its comparatively less complex manufacturing process than the full coaxial one, less expensive associated data acquisition system, and less expensive multislit collimator. These factors will eventually help in having a full device ready for demonstration in comparatively less time so that the different aspects of the segmented HPGe detector for GET measurement could be experimentally validated/evaluated such as detection efficiency, data analysis methods, and count rate capabilities. Even though the demonstration device is different in size and shape, the principle of operation (data acquisition and analysis) is similar to the full coaxial one. The spatial response of the demonstration detector was evaluated. For this purpose, the modulation transfer function (MTF) was chosen as a performance parameter [8], [9]. Simulations were performed using the particle transport code MCNP6.2 [10] to obtain the line spread function (LSF) whose Fourier transform constitutes the MTF curve. Furthermore, to demonstrate the performance, tomographic reconstructions were also made from the simulated projection data of simplified symmetric test object inspections.

II. Design and Working Principle of the Proposed Detector

The proposed detector is a planar, electronically segmented HPGe detector whose front electrode is segmented to obtain seven segments as shown schematically in Fig. 1. The six small
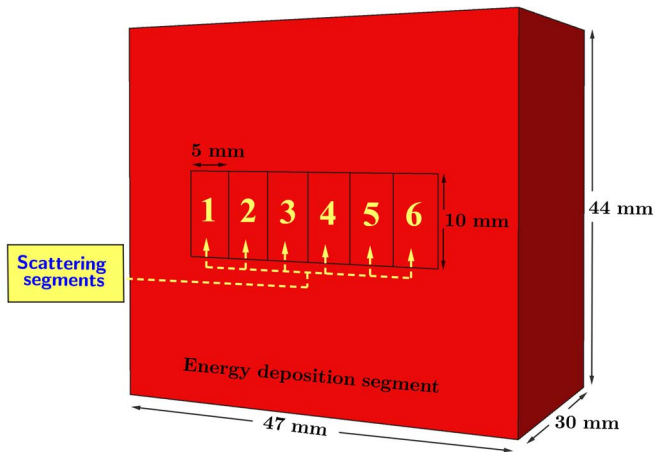
Fig. 1. Proposed planar electronically segmented HPGe detector. The front electrode of the detector is segmented into a total of seven segments.
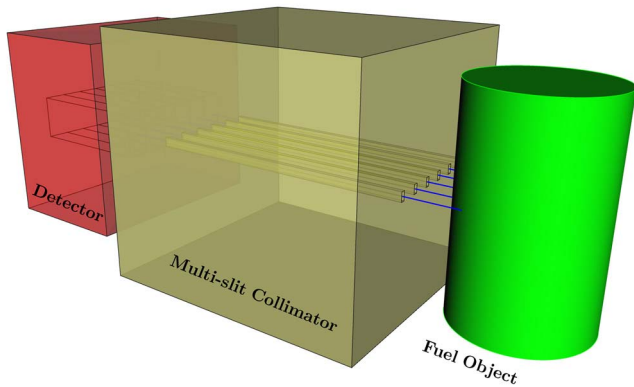

Fig. 2. Illustration of the detector and multislit collimator setup during GET measurement.

equal-sized segments are named "scattering segments," and the rest of the portion is named "energy deposition segment." The naming convention of the segments is similar to the one used in [3]. The back electrode is unsegmented and a high-voltage bias is applied to this electrode. The signals from each segment of the detector and from the unsegmented back electrode are read using a high-speed digitizer. The outer dimensions ($w \times h \times d$) of the detector are 47 mm $\times$ 44 mm $\times$ 30 mm, and each scattering segment is 10 mm in height, 5 mm in width, and 30 mm in depth.

The experimental arrangement of the detector system during a foreseeable GET measurement is illustrated in Fig. 2. As shown in the figure, a multislit collimator is used whose slits are aligned with the scattering segments, and each slit only irradiates its respective scattering segment. Each slit of the collimator defines the volume of the fuel object being measured, and the collimator–detector system moves together to perform a full lateral scan of the object. The number of counts at each measuring position is obtained through the analysis of the signal data obtained from each segment and the back electrode. The proposed data analysis method, which is also used in the simulations, is as follows.

1) An event is assigned to a scattering segment and, thus, to the corresponding slit only if there is a net signal

in that scattering segment. Transient signals (net zero, during the experiment) from the neighboring scattering segments due to the induced mirror charges are ignored for this purpose [and are not simulated with Monte Carlo N-Particle (MCNP)]. The deposited energy information for the event can be obtained through the back electrode signal or summing the coincidence signals from the scattering segment and the energy deposition segment, which may have received a fraction of the gamma-ray energy due to multiple scattering.

2) If there are net signals, in coincidence, from more than one scattering segment, then such events are discarded to avoid the ambiguity of slit localization.

III. SPATIAL RESPONSE OF THE DETECTOR

The spatial response of the segmented detector–collimator system to a photon-emitting object, e.g., a fuel rod, was studied and the achievable spatial resolution was quantified. This will aid in designing the experimental setup, including the design of the collimator, and fixing other relevant parameters. The spatial resolution was quantified with the MTF which is widely used [8], [9], [11] to quantify the spatial resolution for imaging systems.

The MTF describes how the spatial variations in the intensity are transferred from the object to the image obtained through an imaging device, as a function of the spatial frequency in the object. The MTF typically has values ranging from 1 to 0 as a function of the spatial frequency, meaning 100% contrast transfer (ideal) to 0% contrast transfer at the respective spatial frequency. To obtain the MTF curve for the collimated detector system, the LSF method was used. This implies that.

1) A line source was scanned laterally and the full-energy peak counts were obtained at each position (as obtained using the data analysis method of Section II) to obtain the LSF. In the MCNP simulations, the full-energy counts were obtained as the probability of full-energy deposition per source particle; after taking into consideration the source activity, the counts per unit time were provided.

2) The Fourier transform of the LSF was calculated, and the MTF curve was obtained.

In addition to the MTF, a few tomographic reconstructions were also made from the simulated data (obtained from scanning the test objects using MCNP) and using the filtered back projection (FBP) method to reconstruct the activity distribution of the object. The test objects were selected to aid the analysis of the performance in terms of spatial resolution of the system. The details of the simulations performed are given in Section IV.

IV. SIMULATION STUDY

The geometry of the segmented detector and the multi-slit collimator, proposed to be made of Densimet[1] (density: 17.6 g/cm^3), was modeled and simulated using the particle
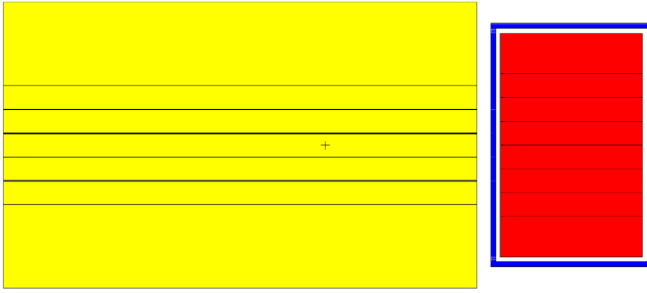
[1]Registered Trademark.

Fig. 3. Plot (horizontal plane view) of the modeled geometry in MCNP from one of the simulations. The source/object was located to the left of the collimator.

transport code MCNP6.2. The dimensions of the detector used in the simulations are as shown in Fig. 1 with the addition of the 1-mm-thick aluminum detector enclosure. The length of the collimator was varied in the LSF simulations, but in the reconstruction simulations, only one collimator length was evaluated. For reference, a cross-sectional view of the modeled geometry from one of the simulations is given in Fig. 3. In all the simulations, both photon and electron transport and the default physics options [12] were used except for bremsstrahlung photon generation which was turned off to reduce the computational time (the difference in the MCNP simulation output due to this was less than 2% as observed in a test simulation). The F8 pulse height tally (modified according to the coincidence and anticoincidence logic) was used in the simulations which is analogous to a physical detector. The F8 [12] tally provides the energy distribution of pulses created in the region that models the segmented HPGe detector along with the statistical relative error for each energy bin. F8 tally results provide only the probability per source particle for each energy bin; to convert the tally result into counts, it has to be multiplied by the source activity. We do not consider nonlinearities of the pulse height response, but this is rather negligible with HPGe detectors. Gaussian broadening of peaks was not considered in the MCNP tally; however, the width of the simulation energy bin was 2 keV, which corresponds well to a typical peak width in HPGe.

Primarily, three different simulation studies were performed, and their details are given in Sections IV-A–IV-C.

A. Intrinsic Full-Energy Efficiency

The main purpose of having the electronic segmentation is to achieve simultaneous detection of photons that enter into the scattering segments after traveling through the respective collimator slits, as if we are using physically separate detectors and counting the photons from each respective slit. In the simulations, this was achieved using the data analysis method as described in Section II. An important thing to note here is that the anticoincidence/coincidence logic was applied to the measured spectra using the tools available in MCNP6.2 to mimic the data analysis method in the simulations.

To evaluate the performance of the individual scattering segments in terms of the intrinsic full-energy detection efficiency,

simulations were performed by modeling the full detector without the collimator and irradiating only the scattering segments by a point monoenergetic gamma-ray source located at a distance of 20 mm from the detector front face. Each scattering segment was irradiated in separate simulations. The intrinsic full-energy efficiency, which is defined as the probability of full-energy deposition per incident source particle on the scattering segment, was obtained from the simulated spectra from each simulation. The intrinsic total spectrum efficiency was also evaluated, obtained by summing the probabilities over all energy bins. The number of photon tracks used in each simulation was 10^8.

B. Line Spread Function

To obtain the LSF, simulations were performed in which a vertical line source was scanned by moving the collimated detector system in small steps horizontally in front of the line source and obtaining the full-energy peak counts per source particle at each position from the pulse height spectra.

The line source was modeled at a 10-mm distance from the collimator face and in front of the slit aligned with the scattering segment-3 (see Fig. 1). The height of the line source was 5 mm which was 0.5 mm longer at both ends compared with the slit height (4 mm). The emission angle from the line source was not isotropic, rather source photons were emitted in the forward direction toward the collimator to save the computation time. The emission angle covered a 160° spread which means the emitted photons from the line source can irradiate all the four corners of the collimator front face. The energies of the photons in the simulations were 662 and 1596 keV, which are representative of the studies of irradiated fuel [13]–[16].

Two sets of LSF values were obtained for two different collimator lengths, 100 and 150 mm with a rectangular slit of size 0.1 mm (width) × 4 mm (height). The pulse height spectra were obtained from the simulations at a stepping interval of 0.05 mm, and 2×10^{10} photon tracks were simulated at each step.

C. Test Object Reconstructions

For the test object reconstructions, a few simulations were performed with the geometry modeled in a manner as shown in Fig. 4. The test objects were modeled as concentric UO_2 cylinders of density 10.98 g/cm^3 and a varying gap width in between according to Table I to provide suitable test features for tomographic reconstruction. For the illustration purpose, ideal tomograms are shown in Figs. 5 and 6 for object-1 and object-2, respectively.

The objects were scanned laterally by moving the collimator–detector system in steps (see Table I), and the probability of full-energy deposition per source photon at each position and for each scattering segment was obtained from the pulse height spectra after applying the anticoincidence/coincidence logic to construct the projection data.

A few simplifications were assumed in the simulations for the reconstruction tests to speed up the simulations and save time. First, photon emission was forward-biased with
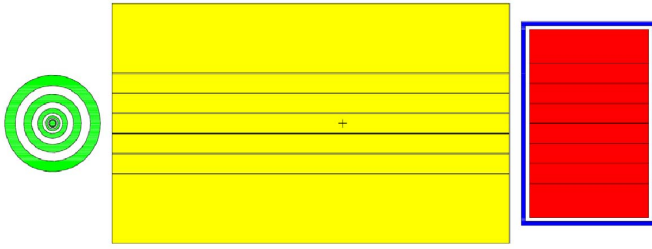
Fig. 4.   Horizontal cross section of the MCNP model geometry for the test object reconstruction tests. The test objects (in green color) were modeled as concentric cylinders of UO_2 material with a density of 10.98 g/cm^3.
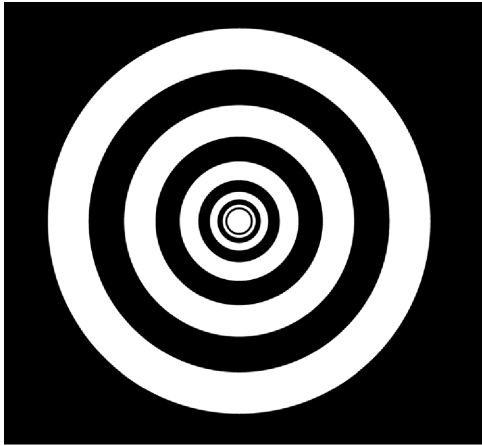

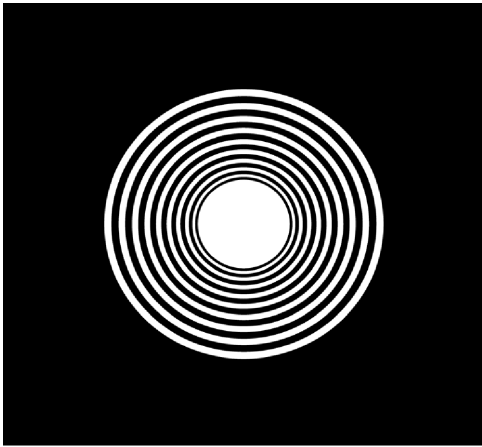Fig. 5.   Illustration of ideal tomogram of object-1.

Fig. 6.   Illustration of ideal tomogram of object-2.

TABLE I
SIMULATION PARAMETERS FOR TEST OBJECT RECONSTRUCTIONS

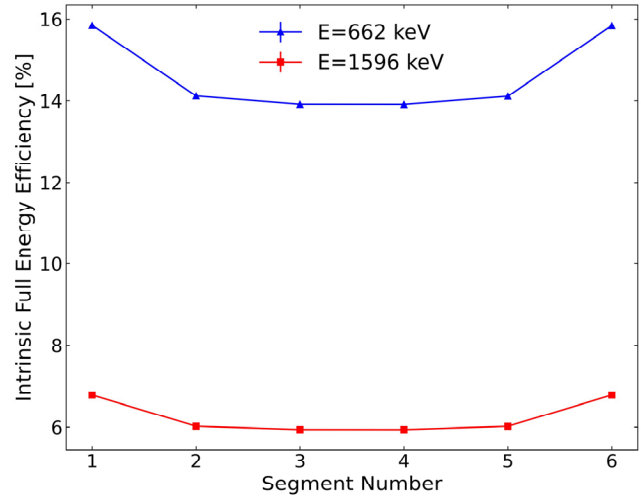| Object diameter (mm)	Size range of inner object gaps (mm)	Collimator length (mm)	Slit width (mm)	Step size (mm)	Photon energy (keV)
Object -1 24.1	0.1 − 2.2	100	0.2	0.2	662
Object -2 12.1	0.1 − 0.3	100	0.2	0.2	662
			0.1	0.1	662

Fig. 7.   Intrinsic full-energy efficiency for each scattering segment/detection element at 662 and 1596 keV.

For test reconstructions, 3×10^{10} photon tracks (monoenergetic, 662 keV) were simulated in each step, and other details about the simulated test objects and simulation parameters are given in Table I.

V. RESULTS

A. Intrinsic Full-Energy Efficiency

The intrinsic full-energy efficiency for each detection element/scattering segment at 662 and 1596 keV was plotted and is shown in Fig. 7. The efficiency varies between 14% and 16% at 662 keV and 6% and 7% at 1596 keV, and the efficiency in segment numbers 1 and 6 is higher. This might have been expected, since these segments are adjacent to the energy deposition segment and it is more likely that the scattered photons from these segments enter into the energy deposition segment and deposit full energy, as opposed to entering a neighboring scattering segment, which may trigger the anticoincidence veto.

For comparison, the full-energy efficiency of the whole detector (as being unsegmented) was also obtained through simulations which at 662 keV is approximately 23% and at 1596 keV is approximately 11%. While this efficiency is higher than the single segment efficiency, the simultaneous utilization of six segments more than compensates for this

an angular divergence of 0.5°. An additional simplification for reducing the computation time was to use rotationally symmetric test objects. Therefore, only one projection was required at 0° rotation, and for the projection data at all the other angles, the same data were repeated to form a full sinogram.

To obtain realistic counting noise affecting the reconstruction, Poisson-distributed noise was added to the projection data of each data point in the sinogram.
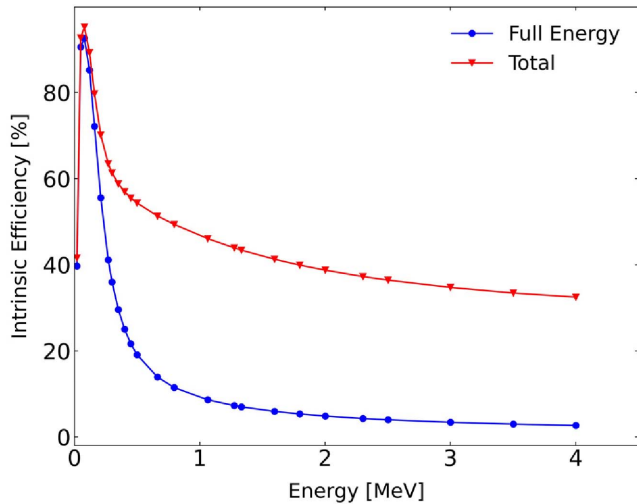
Fig. 8. Efficiency response curve for scattering segment-3/detection element-3.

reduced efficiency of the individual segment by collecting data in six channels in parallel. For the particular case of 662-keV photons, the segmented HPGe detector would be $3.7 = (6 \times 14/23)$ times faster in comparison to an unsegmented HPGe detector of the same overall dimensions, therefore more than compensating for the lower efficiency with the larger number of detection elements.

The energy efficiency response curve for scattering segment number 3 at different incident photon energies was obtained in separate simulations and is shown in Fig. 8. Both total and full-energy intrinsic efficiencies were plotted as a function of energy.

B. LSF and the MTF Curve

Two sets of LSFs were obtained for the two different collimator lengths, 100 and 150 mm, according to Section IV-B. The LSFs for the two cases were plotted and are shown in Figs. 9 and 10, respectively. The MTF curves for the two cases were obtained by taking the Fourier transforms of the LSFs which were plotted versus line pairs per millimeter as shown in Figs. 11 and 12 for the collimator of lengths 100 and 150 mm, respectively.

For the shorter collimator (100 mm), the LSF at higher photon energy (1596 keV) has tails that asymptotically approach nonzero values (Fig. 9), meaning that some of the high-energy gamma rays penetrate the collimator bulk. The effect of this on the MTF can also be noted as shown in Fig. 11, where the 100-mm collimator shows much reduced performance for the 1596-keV photons when compared with 662-keV photons. On the other hand, for the 150-mm-long collimator, these tails of the LSF are almost zero also at 1596 keV, and a better contrast was thus obtained in the MTF.

The limiting resolution of the collimated detector system was obtained from the MTF curve at MTF30, which corresponds to the line frequency where 30% contrast is transferred.

The spatial frequencies at MTF30 for both the collimators and at both photon energies, 662 and 1596 keV, were obtained and used to quantify the spatial resolution. Since the spatial
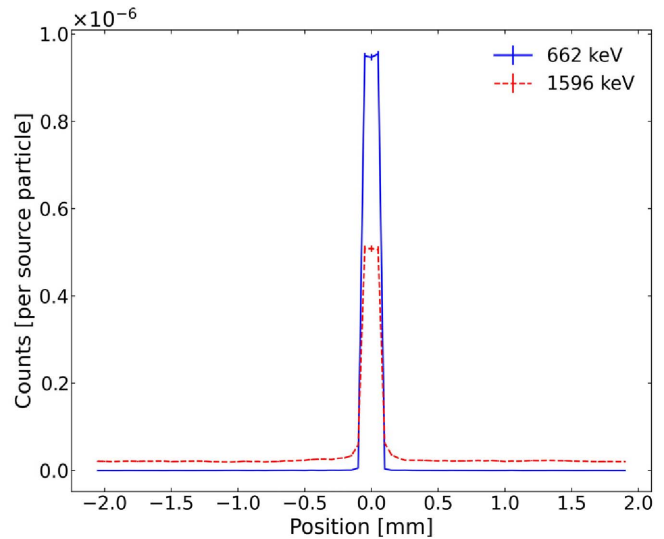

Fig. 9. LSF for collimator of length 100 mm which shows the distribution of full-energy counts at 662 and 1596-keV photon energies in the perpendicular direction of a line source. The error bars represent the one-sigma estimated uncertainties in the values from the MCNP results.
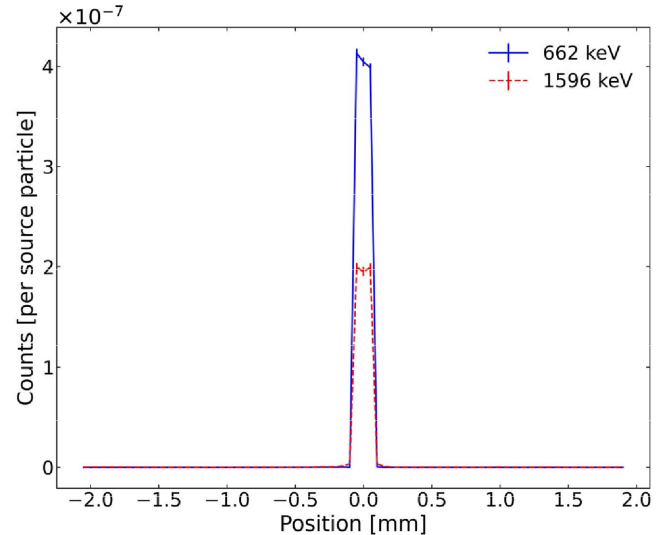

Fig. 10. LSF for collimator of length 150 mm. The error bars represent the one-sigma estimated uncertainties in the values from the MCNP results.

frequency is measured in line pairs per millimeter, the spatial resolution was obtained as $1/(2 \times \text{spatial frequency})$. The spatial resolution for the 100-mm-long collimator at 30% contrast was thus obtained as 0.1 and 0.16 mm for 662 and 1596 keV photons, respectively. The spatial resolution for the 150-mm-long collimator was obtained almost equal (0.1 mm) at both photon energies.

C. Test Object Reconstructions

The projection data for test object reconstructions were obtained by analyzing the spectra from each scattering segment. For test object-1, the single projection at projection angle 0° was plotted and is shown in Fig. 13(a). In total, 150 (25 positions × 6 detection elements) lateral positions were simulated, and the full-energy counts per source particle were obtained.
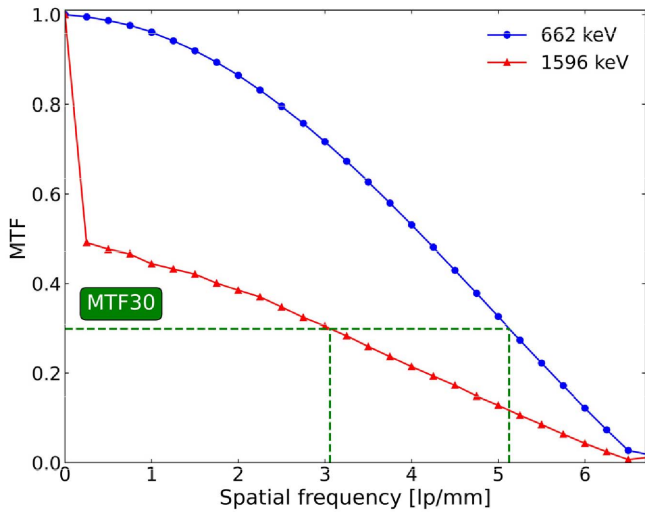
Fig. 11.   MTF curve for a collimator of length 100 mm. The MTF30 value corresponds to the spatial resolution at 30% contrast transfer.
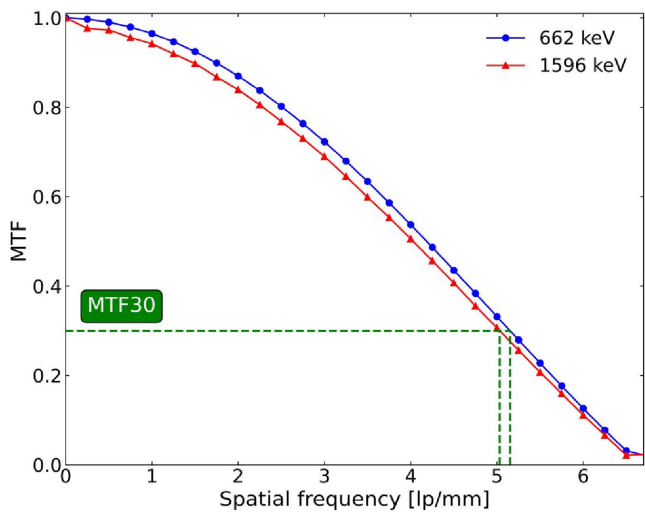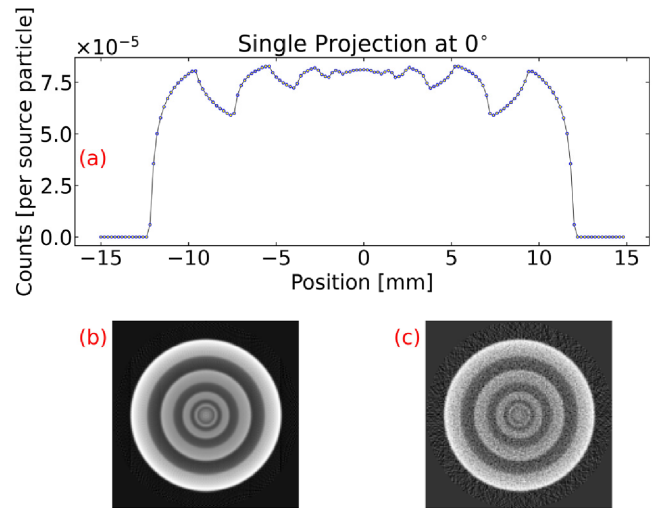

Fig. 13.   Test object reconstructions. (a) Single projection plot at 0° for object-1. (b) Reconstructed image of object-1. (c) Reconstructed image with added Poisson counting noise to the projection matrix before reconstruction.

Fig. 12.   MTF curve for a collimator of length 150 mm.

Fig. 14.   Test object reconstructions. (a) Single projection plot at 0° for object-2, step size = 0.2 mm, and slit width = 0.2 mm. (b) Reconstructed image of object-2. (c) Reconstructed image with added Poisson counting noise to the projection matrix before reconstruction.

It should be noted that from the simulated spectra one just obtains the probability of full-energy deposition per source particle, and therefore, to get the total counts at each position we have multiplied the projection data by a factor such that at the central scan position approximately 1000 counts should be obtained after multiplication. It was assumed that a minimum of 1000 counts (based on a previous tomographic reconstruction experience of nuclear fuel object [17]) at this position would be required to have a satisfactory reconstruction; also assuming the counts as Poisson-distributed, this would result in uncertainty of ±3%. This was done for all the reconstruction cases.

The images were reconstructed using the FBP algorithm with a ramp filter from the scikit image processing [18] module in Python. The reconstructed images are shown in Fig. 13(b) and (c). The reconstructed image in Fig. 13(b) was obtained by repeating the same projection data at 150 equiangular rotational positions distributed in 2π and making the reconstruction with the sinogram thus obtained. To obtain the

image shown in Fig. 13(c), Poisson noise was added to the sonogram, and then the image was reconstructed.

In the first scan of test object-2, a total of 150 lateral positions were scanned with 0.2-mm-wide slits with a step size of 0.2 mm. The same procedure (as used in the test object-1 case) was used to make the reconstructions, and the reconstructed images are shown in Fig. 14(b) and (c) as obtained without and with added Poisson noise, respectively.

In the second scan of test object-2, the step size and the slit width were decreased from 0.2 to 0.1 mm. Therefore, in total 300 (50 positions × 6 detection elements) lateral positions were scanned, and the full energy counts per source particle were obtained. The reconstructions are shown in Fig. 15(b) and (c) as obtained without and with added Poisson noise, respectively. As can be seen in Fig. 16, which is the plot of the central slices of the reconstructed images from the two scans, the features are more resolved in the second scan for the
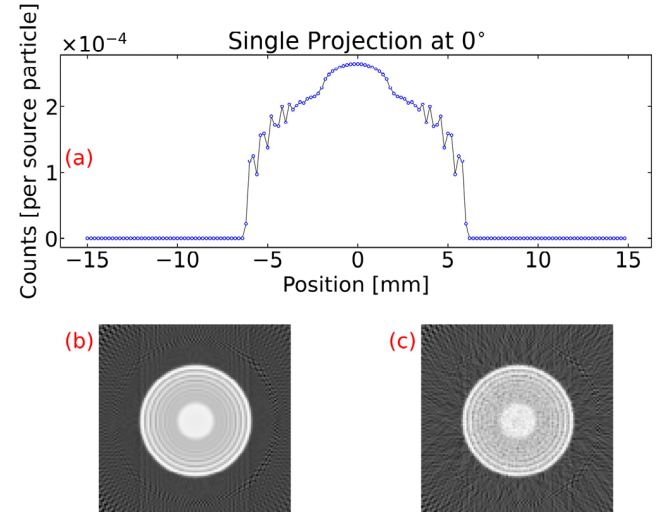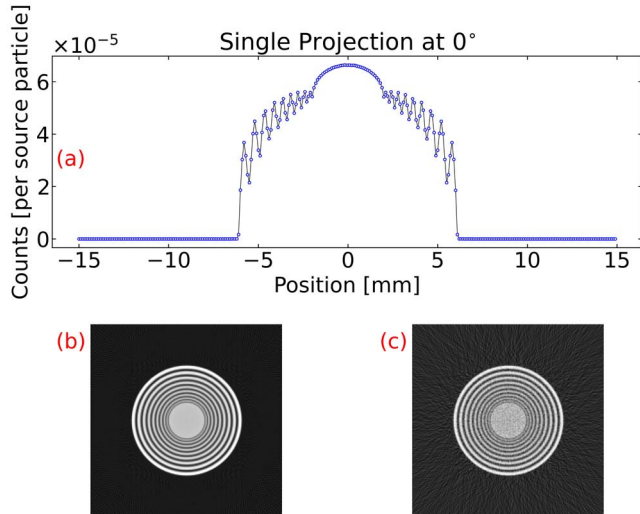
Fig. 15.   Test object reconstructions. (a) Single projection plot at 0° for object-2, step size = 0.1 mm, and slit width = 0.1 mm. (b) Reconstructed image of object-2. (c) Reconstructed image with added Poisson counting noise to the projection matrix before reconstruction.
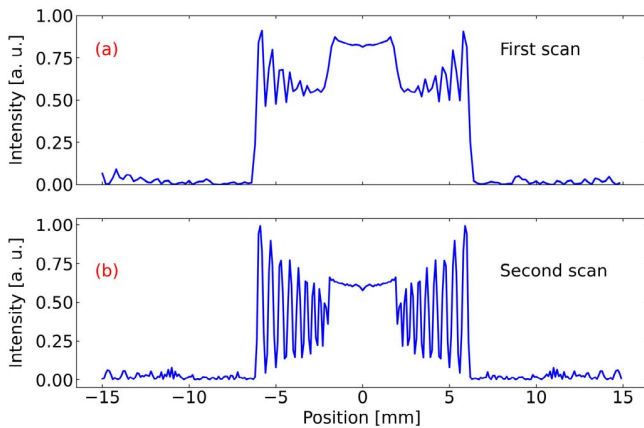

Fig. 16.   (a) Central slice plot of the reconstructed image [Fig. 14(b)]. (b) Central slice plot of the reconstructed image [Fig. 15(b)].

quite obvious reason of having more projection data. However, more time needs to be spent during an experimental measurement to acquire this amount of projection data as illustrated below. The obtainable resolution may thus be limited by time constraints.

For example, simulations were performed to roughly estimate the required time to complete a 2π scan of a 30-mm diameter UO_2 object with around 2.2×10^{11} photons/cm/s initial activity (of ^{137}Cs, 662 keV, from 60 MWd/kg burnup) at one axial location with different collimator slits and step sizes. Again, the total time was calculated by assuming a minimum of 1000 counts at the central scan position. The number of angular rotation steps of the object was assumed equal to the number of lateral measuring positions. A 100-mm-long collimator was used in all the simulations, and for comparison, the required time for one case is given in Table II. The required time increases manifold as the slit size and the step size are halved as given in the table. This increase in time is reasonable since the measuring positions are fourfold, and in addition

TABLE II
ROUGH ESTIMATE OF THE TOTAL REQUIRED TIME FOR AN AXIAL SCAN

Cooling time – 2 days				
Slit size (w × h) (mm)	Step size (mm)	Total lateral steps at each angle	Total angular steps	Total time required (hours)
0.1 × 2	0.1	300	300	257
0.2 × 2	0.2	150	150	18

the optical-field-of-view [19] is four times smaller, leading to an increase in the total scan time by a factor of 16, when compared with a factor of 14.3, which was obtained using the MCNP simulation count rates instead.

VI. CONCLUSION

The spatial response of a collimated segmented HPGe detector was obtained from the simulation study using particle transport code MCNP6.2. The LSF and the MTF were obtained for two different lengths of the multislit collimator. The limiting spatial resolution obtained for 30% contrast is approximately the same as the width of the slit (0.1 mm) for 662-keV photons and 0.16 mm for 1596-keV photons with a 100-mm-long collimator. The values of the limiting resolution improve with a 150-mm-long collimator, especially for 1596-keV photons. For a shorter collimator, the transmission of high-energy photons through the collimator material and slit corners deteriorates the LSF and subsequently the MTF.

Test object reconstructions were made using projection data obtained from the simulations of simplified symmetrical test objects. These simplifications were used to save the computation time; still, these reconstructions exhibit the viability and performance of the segmented HPGe detector for GET measurements. However, it should be noted that in realistic measurements on nuclear fuel in test reactors, the activity of the sample may vary by many orders of magnitude, depending on whether high-burnup fuel is studied, or on the opposite extreme, fresh fuel exposed only to the reactor pulse of in-pile transient tests. Collimator selection and experimental settings such as step size and measurement time per position should thus be adapted to the activity of the sample. Development of methods to facilitate such adaptions, experiment design, and planning is ongoing.

The detector is currently in the manufacturing phase and is likely to be installed in early 2022, and the experimental validation of the results will be carried out after the installation. Eventually, the detector will be available for the postirradiation examination of irradiation-tested fuel samples.

VII. OUTLOOK AND DISCUSSION

The choice of a collimator is dictated by the spatial resolution requirements at the photon energies of interest; using a longer collimator certainly helps in achieving a better spatial resolution but it is not always possible as it can prolong the measurement duration, due to lowering the count rate. Using the two different lengths (100 and 150 mm) in the simulations, we have shown that the obtainable spatial resolution is similar for the 662-keV case but greatly improves

for the 1596-keV case. The final choice of the collimator will depend on the source activity, isotope of interest, and time for measurement. Thus, if interested only in the 662-keV photons in a long-cooled fuel that lacks the 1596-keV peak, we might be better off using the shorter collimator, which obtains a higher count rate. Depending on the circumstances, different collimators can be used, and for that matter, the results from the simulations will be crucial to design the experiments.

In our study, we have considered spatial resolution only in the lateral direction considering many fuel objects may have some symmetry in the axial direction (thus the height of the collimator slit can be taken larger than the width), but it is also worth mentioning that the spatial resolution in the axial direction may also be important particularly in cases where the fuel inside the cladding is fragmented and may not have axial symmetry. In such cases, slit height needs to be adjusted according to the measurement requirements. For the test objects' reconstructions, only two representative photon energies were used, but it should also be noted that the spent fuel emits photons of many different energies. In such cases, peaks may overlap or scatter background may hinder the determination of some peaks, but considering the excellent energy resolution of HPGes and availability of fast data acquisition systems, this is not expected to be a significant issue.

In this work, the required time to complete the scan was calculated for a representative burnup case of 60 MWd/kg and two representative slit dimensions. The estimated time of 257 h to complete an axial scan with a 0.1-mm-wide slit is indeed a long time, and if one has to scan many axial positions (e.g., in scanning a fragmented fuel that may not have axial symmetry) then it would certainly be very time-expensive although not impossible. However, a reasonable compromise can be obtained using a 0.2-mm-wide slit that can complete one axial scan in less than 24 h. It can be noted that the real measurement time will also be affected by factors such as detector dead time and time losses for movement of the detector relative to the fuel object. Therefore, in the future, all the factors which introduce uncertainty in the total scan time required need to be considered and analyzed. Furthermore, it is also planned for using different reconstruction methods to analyze the effect on the quality of the reconstructed image.

Even though the demonstration scaled-down detector version has only six scattering segments and the primary objective of using it is to evaluate the capabilities of the novel segmented HPGe detector concept for spent fuel measurements, we also envision some use cases of the device. In particular, fuel objects of up to 30-mm width can be covered with a single 5-mm sweep of the detector, by utilization of the six segments. This may be useful, for example, in the inspection of transient fuel test rods, often with the relocation of fuel causing a larger size than nominal fuel rod diameter. Inspections of irradiated fuel assemblies (of larger size) would require repeating several 30-mm scans, each made by moving the segmented detector 5 mm. Even in this case, the segmented detector can speed up data collection or produce data with higher spatial sampling frequency at the same time, compared with an unsegmented detector.

REFERENCES

[1] S. Akkoyun *et al.*, "AGATA—Advanced gamma tracking array," *Nucl. Instrum. Methods Phys. Res. A, Accel. Spectrom. Detect. Assoc. Equip.*, vol. 668, pp. 26–58, Mar. 2012, doi: 10.1016/j.nima.2011.11.081.

[2] S. Paschalis *et al.*, "The performance of the gamma-ray energy tracking in-beam nuclear array GRETINA," *Nucl. Instrum. Methods Phys. Res. A, Accel. Spectrom. Detect. Assoc. Equip.*, vol. 709, pp. 44–55, May 2013, doi: 10.1016/j.nima.2013.01.009.

[3] P. Andersson *et al.*, "Simulation of the response of a segmented high-purity germanium detector for gamma emission tomography of nuclear fuel," *Social Netw. Appl. Sci.*, vol. 2, no. 2, p. 271, Jan. 2020, doi: 10.1007/s42452-020-2053-4.

[4] V. Rathore, L. Senis, E. A. Sundén, P. Jansson, A. Håkansson, and P. Andersson, "Geometrical optimisation of a segmented HPGe detector for spectroscopic gamma emission tomography—A simulation study," *Nucl. Instrum. Methods Phys. Res. A, Accel. Spectrom. Detect. Assoc. Equip.*, vol. 998, May 2021, Art. no. 165164, doi: 10.1016/j.nima.2021.165164.

[5] P. Andersson, S. Holcombe, and T. Tverberg. (Jul. 2016). *Inspection of a LOCA Test Rod at the Halden Reactor Project Using Gamma Emission Tomography*. [Online]. Available: https://www.osti.gov/biblio/22764099

[6] B. Biard, "Quantitative analysis of the fission product distribution in a damaged fuel assembly using gamma-spectrometry and computed tomography for the Phébus FPT3 test," *Nucl. Eng. Des.*, vol. 262, pp. 469–483, Sep. 2013, doi: 10.1016/j.nucengdes.2013.05.019.

[7] J. Schulthess *et al.*, "Non-destructive post-irradiation examination results of the first modern fueled experiments in TREAT," *J. Nucl. Mater.*, vol. 541, Dec. 2020, Art. no. 152442, doi: 10.1016/j.jnucmat.2020.152442.

[8] B. Juste, R. Miró, P. Monasor, and G. Verdú, "Monte Carlo calculation of the spatial response (modulated transfer function) of a scintillation flat panel and comparison with experimental results," *Radiat. Phys. Chem.*, vol. 116, pp. 181–185, Nov. 2015, doi: 10.1016/j.radphyschem.2015.01.005.

[9] J. Diaz, T. Kim, V. Petrov, and A. Manera, "X-ray and gamma-ray tomographic imaging of fuel relocation inside sodium fast reactor test assemblies during severe accidents," *J. Nucl. Mater.*, vol. 543, Jan. 2021, Art. no. 152567, doi: 10.1016/j.jnucmat.2020.152567.

[10] C. J. Werner, Ed., "MCNP6.2 release notes," Los Alamos Nat. Lab., Los Alamos, NM, USA, Tech. Rep. LA-UR-18-20808, 2018.

[11] A. Gopal and S. S. Samant, "Validity of the line-pair bar-pattern method in the measurement of the modulation transfer function (MTF) in megavoltage imaging," *Med. Phys.*, vol. 35, no. 1, pp. 270–279, Jan. 2008, doi: 10.1118/1.2816108.

[12] C. J. Werner, Ed., "MCNP users manual—Code version 6.2," Los Alamos Nat. Lab., Los Alamos, NM, USA, Tech. Rep. LA-UR-17-29981, 2017.

[13] S. Holcombe, S. Jacobsson Svärd, and L. Hallstadius, "A novel gamma emission tomography instrument for enhanced fuel characterization capabilities within the OECD Halden reactor project," *Ann. Nucl. Energy*, vol. 85, pp. 837–845, Nov. 2015, doi: 10.1016/j.anucene.2015.06.043.

[14] S. Caruso, M. Murphy, F. Jatuff, and R. Chawla, "Validation of ^{134}Cs, ^{137}Cs and ^{154}Eu single ratios as burnup monitors for ultra-high burnup UO$_2$ fuel," *Ann. Nucl. Energy*, vol. 34, nos. 1–2, pp. 28–35, Jan. 2007, doi: 10.1016/j.anucene.2006.11.009.

[15] P. Jansson, S. J. Svärd, A. Håkansson, and A. Bäcklin, "A device for nondestructive experimental determination of the power distribution in a nuclear fuel assembly," *Nucl. Sci. Eng.*, vol. 152, no. 1, pp. 76–86, Jan. 2006, doi: 10.13182/NSE06-A2565.

[16] C. Willman, A. Håkansson, O. Osifo, A. Bäcklin, and S. J. Svärd, "Nondestructive assay of spent nuclear fuel with gamma-ray spectroscopy," *Ann. Nucl. Energy*, vol. 33, no. 5, pp. 427–438, Mar. 2006, doi: 10.1016/j.anucene.2005.12.005.

[17] P. Andersson and S. Holcombe, "A computerized method (UPPREC) for quantitative analysis of irradiated nuclear fuel assemblies with gamma emission tomography at the Halden reactor," *Ann. Nucl. Energy*, vol. 110, pp. 88–97, Dec. 2017, doi: 10.1016/j.anucene.2017.06.025.

[18] S. van der Walt *et al.*, "Scikit-image: Image processing in Python," *PeerJ*, vol. 2, p. e453, Jun. 2014, doi: 10.7717/peerj.453.

[19] L. Senis *et al.*, "Evaluation of gamma-ray transmission through rectangular collimator slits for application in nuclear fuel spectrometry," *Nucl. Instrum. Methods Phys. Res. A, Accel. Spectrom. Detect. Assoc. Equip.*, vol. 1014, Oct. 2021, Art. no. 165698, doi: 10.1016/j.nima.2021.165698.